

Research Article

Propulsive Efficiency of Ridge/Inlet Configuration

Guoping Huang,¹ Eiman B. Saheby ,¹ and Anthony Hays²

¹College of Energy and Power, Nanjing University Aeronautics and Astronautics, 29 Yuda St., Nanjing 210016, China

²Department of Mechanical and Aerospace Engineering, California State University, Long Beach, CA 90840, USA

Correspondence should be addressed to Eiman B. Saheby; eimansaheby@yahoo.com

Received 21 January 2018; Revised 7 May 2018; Accepted 3 July 2018; Published 19 August 2018

Academic Editor: William W. Liou

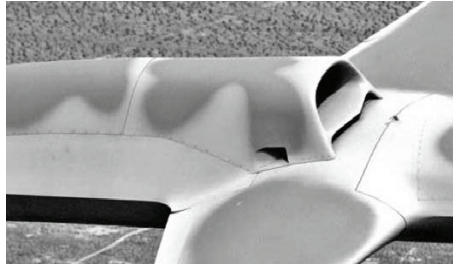
Copyright © 2018 Guoping Huang et al. This is an open access article distributed under the Creative Commons Attribution License, which permits unrestricted use, distribution, and reproduction in any medium, provided the original work is properly cited.

Controlling and directing the boundary layer on the surfaces of a flight vehicle are two of the most demanding challenges in advanced aerodynamic designs. The design of highly integrated and submerged inlets with a large offset between the entrance and compressor face is particularly challenging because of the need for controlling or reducing the adverse effects of the boundary layer on propulsive efficiency. S-duct diffusers are used widely in flight vehicles when the compressor face needs to be hidden, and their performance is generally sensitive to the quality of ingested boundary layer from the fuselage. Passive or active flow control mechanisms are needed to prevent flow separations at the bends. In this paper, a new method is presented for optimal inlet/body integration based on a pair of ridges ahead of the inlet and its effects on the performance of a semicircular S-duct inlet integrated on a flat surface using CFD. In this design, the ridge changes an inefficient inlet concept to one with acceptable performance. The new method of integration is practicable for top-mounted inlet configurations where the use of diverters and other mechanisms results in higher amounts of drag, weight, and complexity.

1. Introduction

Highly integrated inlet concepts have become an important issue in UAV design studies. The main challenge of inlet/body integration is to prevent the thickened boundary layer on the fuselage from entering into the inlet. Low kinetic energy boundary layer flow and its degradation of inlet performance are particularly problematic. Swirling, flow, distortion, and shock/boundary-layer interactions are common adverse phenomena, related to the nature of boundary layer in airbreathing propulsion systems [1–3]. Up to now, few practical designs and integration methods have been successfully used. For example, the classic diverters, Figures 1(a) and 1(b), provide a gap between the inlet and body of an aircraft which prevent the boundary layer from entering the inlet. However, there are some disadvantages concerning this integration technique, such as high drag, additional structural loads, and extra weight. For top-mounted inlet configurations, the problem is more complicated when the engine is installed in the fuselage and an S-duct guides the flow from the inlet entrance to the compressor face. Such a design suffers from secondary flow generation and additional

pressure recovery losses inside the duct, requiring passive or active flow control [4]. Another problem with stealthy top-mounted inlets on UAVs is the short distance between the inlet entrance and compressor face and the large offset which limits the length of the diverter and degrades external aerodynamic performance [5]. Such a limit in design can be seen in Figure 1(a). To overcome these problems by removing the diverter from the design approach and letting the boundary layer flow into the inlet, fundamental changes are needed in the entrance location, the wetted area in front of it, and the flight vehicle configuration. For example, the combination of a serpentine inlet and bump surface on some stealthy UAVs is a viable solution (Figure 1(c)) but this concept works only for inlets close to the nose of the flight vehicle, where the upstream boundary layer on the fuselage is thin. A better example of highly integrated inlet design can be seen in Figure 1(d) with no diverter. Although the Barracuda system is still under development and there are not many data about its propulsion system, the boundary layer control techniques should be used inside the diffuser duct to prevent flow separation. The challenge is greater for inlet locations on the aft section of the fuselage where the



(a) General Atomics, Avenger [6]



(b) Northrop Grumman, Global Hawk [7]



(c) Boeing, X-47 [8]



(d) EADS, Barracuda [9]

FIGURE 1: Top-mounted inlets on different UAVs.

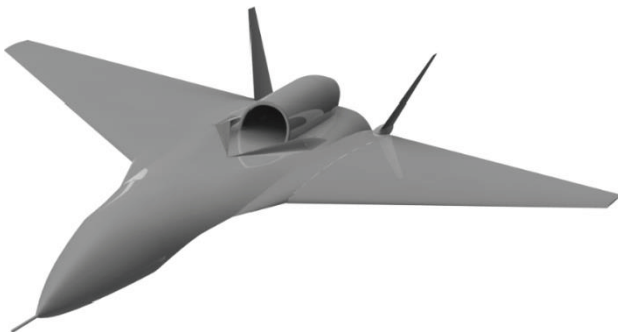


FIGURE 2: Conceptual UAV with ridge/inlet configuration.

boundary layer is thicker. A new concept, called ridge, is therefore proposed for integration of a semicircular inlet mounted on a flat surface. The ridge concept offers a passive solution to this problem as a low-drag and light-weight alternative to a conventional boundary layer diverter. The performance of this design has been analyzed using CFD for concepts with and without a ridge at Mach numbers from 0.3 to 0.8. Figure 2 shows a UAV concept with a ridge/inlet configuration at the aft fuselage location.

2. Designs Philosophy and Geometry

The basic structure of the ridge is shown in Figure 3(a). This shape has been created by lofting geometrically similar cross-sections along oblique lines on a flat surface. These lines determine the diversion path for the boundary layer. The cross-sections have been scaled by a base point scaling algorithm, and the base point is placed on the oblique line in each cross-section plane. Figure 3(b) illustrates the highest cross-section of the ridge. The cross-section is generated from a trimmed circle and two splines, C1 and C2. In this design,

the distance from the center of the circle to the flat plate is a linear function of boundary layer thickness. Other cross-sections are generated by the base point scaling algorithm along the longitudinal axis. The scale factor can be changed based on a quadratic function and provides a steeper ramp for the nose of the ridge. The central surface between the two ridges can be a flat plate and conoid or might be designed based on the inlet entrance geometry. For this concept, an interesting property of the central surface is its flexibility for combining with different compression surfaces and inlet entrances. As mentioned before, the lofting process by CAD software creates the final surface of the ridge in Figure 3 and as a direct result of the scaling algorithm, the front part of the ridge is submerged in the boundary layer on the flat plate. The yellow rear part in Figure 3(a) connects the end of the ridge to the flat surface. The rear section can affect the vortex structure when it leaves the ridge. For example, it can break down the vortex, although this is not a goal in this research.

When this geometry is subjected to high-speed flow, three different pressurized surfaces appear on it: a high-pressure surface (HPS) resulting from surface C1 (in Figure 3(b)), a low-pressure surface (LPS) resulting from C2, and a low-pressure separation band at the tip. Based on these pressurized surfaces, a miniature stable vortex is created along the inboard side of the ridge. This thin vortex starts in the lower part of boundary layer close to the nose of the ridge and grows along the deviation line. The steep pressure gradient between the LPS and HPS causes shear layer separation whose intensity is controlled by the radius of the top of the ridge. This separated flow forms a vortical flow pattern in the vicinity of the low-pressure surface of the ridge.

The boundary layer (BL) streamlines passing over the ridge cannot escape from the vortex. The interaction between the vortex and the BL on the central surface draws the low energy parts of the flow into the low pressure on the inboard

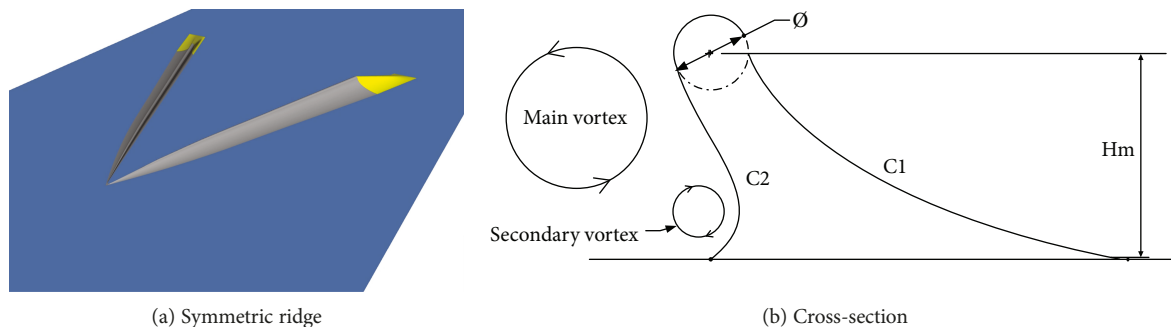


FIGURE 3

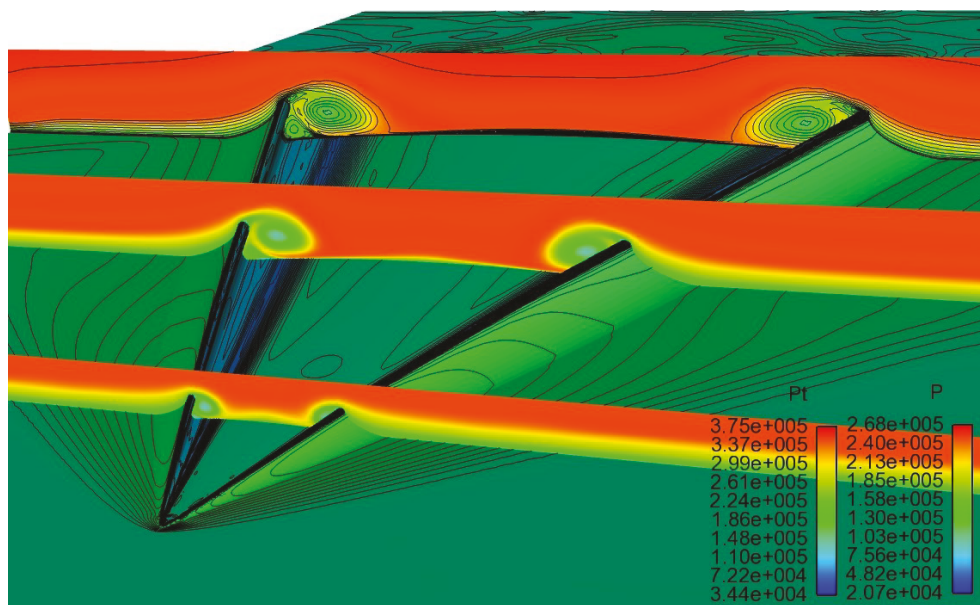


FIGURE 4: Transversal total pressure contours show the vortex structure and boundary layer diversion [1].

side of the ridge. The combination of vortex and steep pressure gradient creates a powerful trap for capturing and diverting the BL from a uniform straight path into a vortical flow pattern along a preset direction. Controlling the vortex based on the aerodynamic characteristics of the ridge is the unique property of this shape. The continual shear layer separation at the ridge constantly adds mass into the vortex structure and decreases the vortex strength. Therefore, the expanding LPS along the oblique line traps the vortex by increasing the height of the ridge along the oblique line. Figures 4 and 5 show the transversal total pressure contours and streamlines around the ridge profile at $M = 1.50$ (close to design limit). The ridge configuration is placed on the center of a flat plate whose upstream length is 20 times that of the ridge. The resultant boundary layer on this plate is very thick at transonic and supersonic speeds. The contours in Figure 4 are the result of the second-order upwind scheme, which predicts a very precise flow pattern around the ridge when the accepted residual accuracy is 10^{-5} . The capability of the ridge to completely capture the boundary layer has been demonstrated by accurate simulations from the low subsonic to low supersonic ($M < 1.7$) regime. Figure 5 shows the vortex by streamlines released near the surface.

Information on advanced concepts based on this design can be found in [1], which focused on the study of external flow patterns of the ridge, and propulsive efficiency of the new configuration was not emphasized. More detailed results of analysis of the basic ridge flow pattern, vortex structures, and other aerodynamic properties of the ridge concept will be published in a future paper. This paper focuses on the effects of the ridge on the internal performance of the integrated inlet.

3. Ridge/Inlet Integration

The candidate inlet for integrating with the ridge configuration is a pitot inlet with a semicircular entrance. Such inlets are becoming common in different flight vehicles, although their integration is not straightforward. In some cases, the curvature of the inlet limits the use of diverters. This problem is more critical for top-mounted inlets, and the designs are limited to a serpentine configuration or aft inlet/diverter configuration. The most important factor involved in this design is aerodynamic performance sensitivity. Bended inlets generally suffer from internal aerodynamic problems such as secondary flow and flow separation after

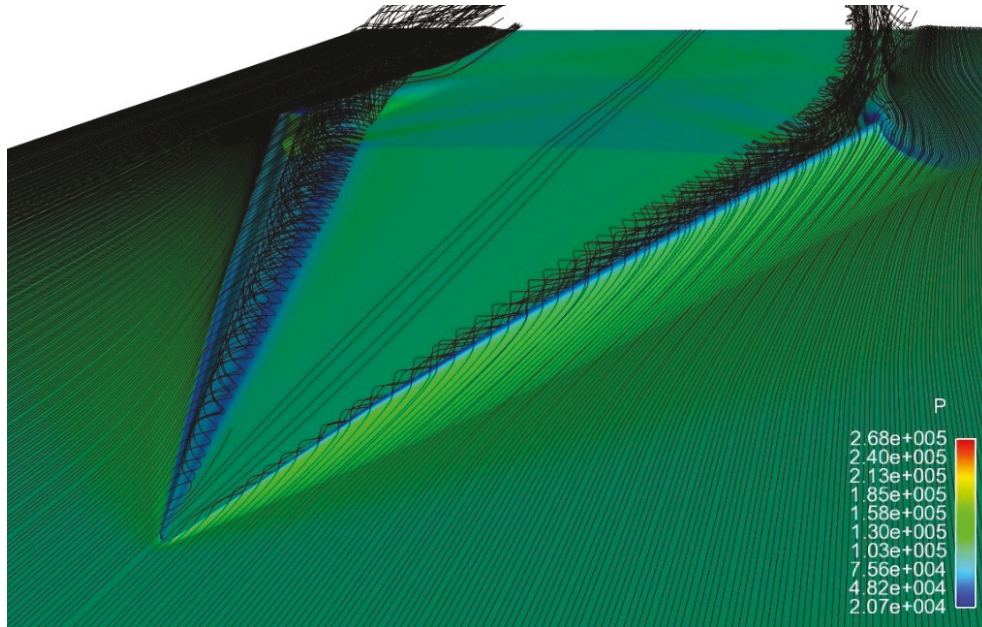


FIGURE 5: Dense group of streamlines released from upstream at $h = 1$ (mm) [1].

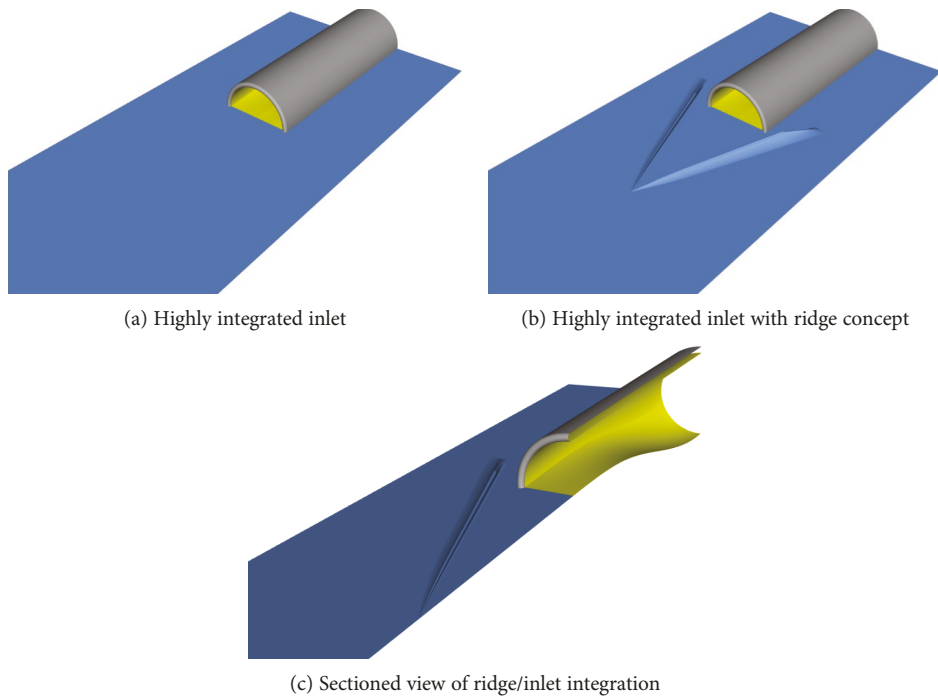


FIGURE 6: Highly integrated inlet with and without ridge on a flat surface, used in CFD simulations.

the first bend of the diffuser. Previous research has shown that the internal aerodynamic performance factors of these diffusers are very sensitive to the resulting flow pattern of the entrance geometry [10, 11]. Such a sensitivity is quite useful to test the effects of the ridge structure on inlet performance.

Figure 6 shows the inlet, with and without ridge on a flat surface. For a reliable numerical simulation, the entrance segments are designed with less complexity; the lip profile is a half-circle with constant radius, and no drag optimization

has been applied to the external surface of the inlet. The diffuser duct is generated by several sections between the entrance and the compressor face. A trigonometric function defines the centerline, and the lofting process by these segments creates the duct surface. The goal of this research is to examine the effects of the integration method, and optimization of the duct profile is not considered. To generate a boundary layer in front of the entrance which is representative of that on a full-scale UAV, a flat plate with a length of 1.7 meters is included upstream of the inlet.

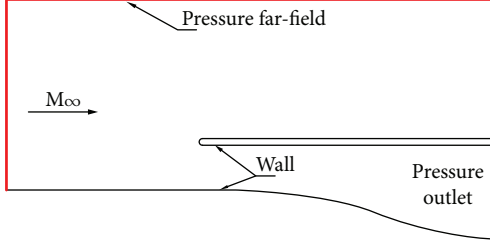


FIGURE 7: Schematic of computational domain and boundary conditions.

The vortex formed by the rollup of the boundary layer must pass to the side of the inlet entrance. The distance between the ridge and entrance provides this passage. Although the diameter of the ridge vortex is smaller than that generated by a wing strake or canard, it must not enter the inlet. Analysis of flow over the ridge at high yaw angles at low subsonic speeds is required to estimate the required gap between the inlet entrance and the ridge. In this paper, CFD simulation results of inlet integration without a ridge have been used to produce a baseline for measurement of the comparative aerodynamic performance of the new concept.

In the previous study [12], the diffuser duct had higher curvature that resulted in some local flow separations after the bend when the inlet was integrated (or reinforced) with the ridge. Such a pattern was experienced when the Mach number exceeded 0.50. In the current investigation, the diffuser duct is designed with less curvature in order to measure the effects of the ridge more accurately by preventing local flow separation related to the duct geometry. The new inlet is designed to measure the effects of the boundary layer from upstream without any extra three-dimensionality inside the inlet.

4. CFD Simulation

The numerical simulations have two primary objectives. The first is to investigate the boundary layer redirecting ability of the ridge with the existence of the inlet entrance on the central surface, especially at high subsonic speeds. Understanding the effects of inlet pressure gradient on the ridge vortex and the stability of the vortex core is the key issue for producing a baseline for aerodynamic testing. The second and most important objective is to investigate the effects of the ridge on the internal flow quality of the S-duct.

Analyzing the boundary layer interactions and related phenomena inside the inlet depends on the abilities of turbulence equations in the numerical solver. An SST turbulence model has been used widely in simulations related to viscous interactions. The model is as economical as the $k-\epsilon$ model, but it offers much higher fidelity, especially for separated flows, providing excellent answers on wide range of flows and near-wall mesh conditions. According to our mesh quality and the existence of viscous interactions in our cases, this turbulence model is a good match with the requirements of this analysis. Previous researchers have proved the

accuracy of this turbulence model for boundary layer analysis [13–16]. In this research, a cluster processor with 4 nodes (32 computational cores) has solved the domain by ANSYS Fluent commercial software and the convergence solution has been accepted when the residuals exceeded 10^{-5} .

4.1. Governing Equations. The governing equations for the present problem are the three-dimensional Navier-Stokes equations. The compact conservation form for these equations are as follows [17, 18].

(i) Continuity equation:

$$\frac{\partial \rho}{\partial t} + \frac{\partial}{\partial x_k} (\rho u_k) = 0, \quad k = 1, 2, 3. \quad (1)$$

(ii) Momentum equation:

$$\frac{\partial}{\partial t} (\rho u_i) + \frac{\partial}{\partial x_k} (\rho u_i u_k) + \frac{\partial p}{\partial x_i} = \frac{\partial (\tau_{ik})}{\partial x_i}, \quad i, k = 1, 2, 3. \quad (2)$$

(iii) Energy equation:

$$\begin{aligned} \frac{\partial}{\partial t} (\rho E) + \frac{\partial}{\partial x_k} (\rho u_k H_t) \\ = - \frac{\partial}{\partial x_i} (u_j \tau_{jk}) + \frac{\partial q_k}{\partial x_k}, \quad i, j, k = 1, 2, 3, \end{aligned} \quad (3)$$

where ρ , u_i , p , E , and H_t are the density, velocity components, pressure, and total energy and enthalpy, respectively. The total energy can be represented by

$$E = e + \frac{1}{2} u_k u_k, \quad (4)$$

where e is the internal energy per unit of mass. H_t is related to the static enthalpy h_s by

$$H_t = h_s + \frac{1}{2} u_k u_k. \quad (5)$$

k is the heat flux related to the conductivity. Turbulent shear stress is defined as

$$\tau_{ik} = \mu \left(\frac{\partial u_i}{\partial x_k} + \frac{\partial u_k}{\partial x_i} \right). \quad (6)$$

$\mu = \mu_1 + \mu_t$ is the total viscosity; μ_1 and μ_t being the laminar and turbulent viscosity. According to the Sutherland formulation, the laminar viscosity (μ_1) is calculated as

$$\mu_1 = \mu_{\text{ref}} \left(\frac{T}{T_{\text{ref}}} \right)^{3/2} \left(\frac{T_{\text{ref}} + S}{T + S} \right), \quad (7)$$

where T is the temperature and μ_{ref} , T_{ref} , and S are known coefficients. In Eddy viscosity models, the stress tensor is expressed as a function of turbulent viscosity (μ_t). Based on dimensional analysis, additional variables (k , ϵ , and ω) are defined as given below.

TABLE 1: Example of acceptable residual accuracy for ridge/inlet configuration.

Number of iterations	Continuity	x velocity	y velocity	z velocity	Energy	k	ω
20,000	8.251×10^{-4}	3.384×10^{-6}	1.079×10^{-5}	3.917×10^{-4}	4.112×10^{-5}	2.328×10^{-4}	4.062×10^{-5}

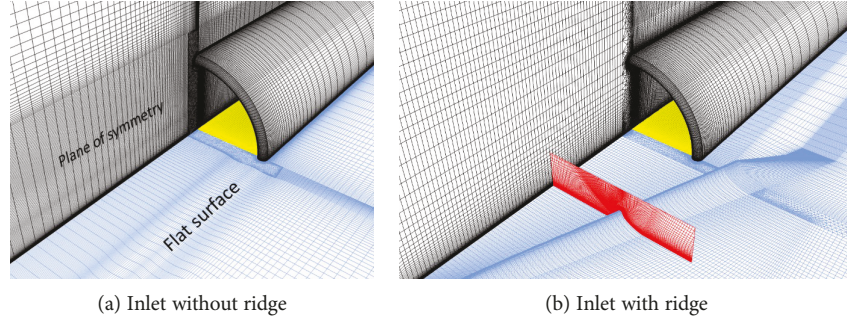


FIGURE 8: Perspective view of surface grid for inlet without ridge profile.

(i) Turbulent kinetic energy k :

$$k = \frac{\overline{u'_i u'_i}}{2}. \quad (8)$$

(ii) Turbulent dissipation rate ε :

$$\varepsilon \equiv \nu \overline{\frac{\partial u'_i}{\partial x_j} \left(\frac{\partial u'_i}{\partial x_j} + \frac{\partial u'_j}{\partial x_i} \right)}. \quad (9)$$

(iii) Specific dissipation rate ω :

$$\omega = \frac{\varepsilon}{k}. \quad (10)$$

The turbulent viscosity, μ_t , is calculated as

$$\mu_t = c_\mu \frac{\rho k^2}{\varepsilon}. \quad (11)$$

The Fluent solver uses a control-volume-based technique to convert a general scalar transport equation to an algebraic equation that can be solved numerically. This control-volume technique consists of integrating the transport equation about each control volume, yielding a discrete equation that expresses the conservation law on a control-volume basis. More information about solver structure may be found in [17]. The turbulent kinetic energy (k) and specific dissipation rate (ω) equations are

$$\begin{aligned} \frac{\partial}{\partial t}(\rho k) + \frac{\partial}{\partial x_i}(\rho k u_i) &= \frac{\partial}{\partial x_j} \left(\Gamma_k \frac{\partial k}{\partial x_j} \right) + \tilde{G}_k - Y_k + S_k, \\ \frac{\partial}{\partial t}(\rho \omega) + \frac{\partial}{\partial x_i}(\rho \omega u_i) &= \frac{\partial}{\partial x_j} \left(\Gamma_\omega \frac{\partial \omega}{\partial x_j} \right) + G_\omega - Y_\omega + D_\omega + S_\omega. \end{aligned} \quad (12)$$

In these equations, \tilde{G}_k represents the generation of turbulence kinetic energy due to mean velocity gradients, G_ω represents the generation of ω , and Γ_k and Γ_ω represent

the effective diffusivity of k and ω , respectively. Y_k and Y_ω represent the dissipation of k and ω due to turbulence. D_ω represents the cross-diffusion term. S_k and S_ω are user-defined source terms [19]. The set of equations explained above are solved simultaneously in the density-based solver.

4.2. Boundary Conditions. A schematic of the computational domain with the boundary conditions is shown in Figure 7. The static back pressure at the pressure outlet causes an adverse pressure gradient inside the inlet where the boundary layer conditions are the function of this boundary condition. Using the two-equation turbulence model in this domain forces the solver to use a CFL number lower than unity for a smooth convergence.

4.3. Numerical Solver. The density-based solver in ANSYS Fluent solves the governing equations of continuity, momentum, and energy simultaneously as a set, or vector, of equations. Governing equations for additional scalars will be solved sequentially (i.e., segregated from one another and from the coupled set). The selected algorithms for solving the coupled set of equations is the implicit formulation [20–22]. The governing equations in Fluent are discretized in time for both steady and unsteady calculations. In the steady case, it is assumed that time marching proceeds until a steady-state solution is reached. The discretizing algorithm at the start of solution is the first-order upwind, and after reaching desired accuracy, it changes to a second-order upwind scheme; then the iterations continue until reaching the desired accuracy. The CFL number less than unity is applied for both parts of iterations. Table 1 shows the residual values at the selected accuracy for a typical case.

4.4. Mesh Generation. For a reliable simulation, a fully structural grid has been created around the ridge and space around the inlet. The y^+ range is between 0.8 and 0.9 on the ridge surface, and the growing rate of cells is 1.10. The three-dimensional Navier-Stokes equations, coupled with a SST turbulence model, can be solved. Because of lateral symmetry, it is possible to reduce computational costs using the boundary conditions at the plane of symmetry. The accuracy

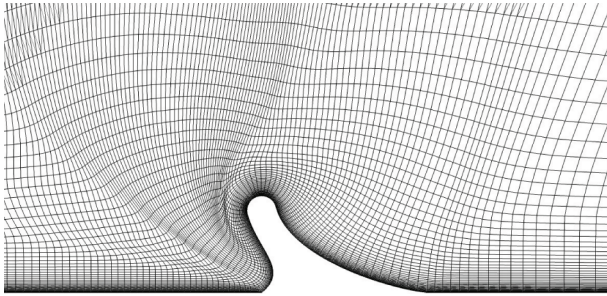


FIGURE 9: Cross-section view of grid structure around the ridge.

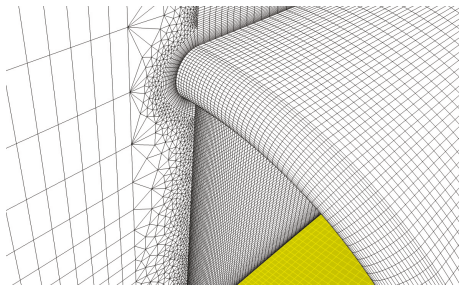


FIGURE 10: Close-up view of the entrance.

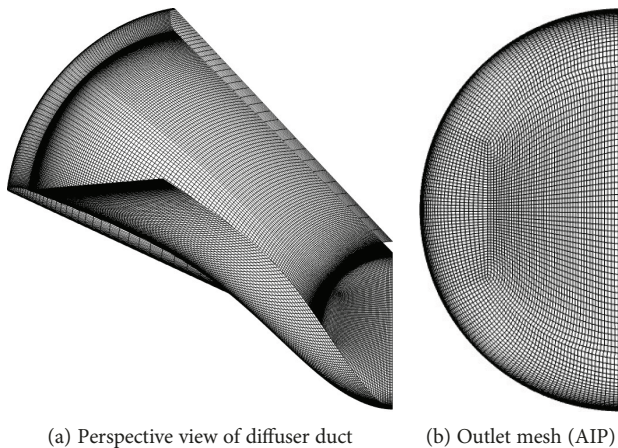


FIGURE 11: Diffuser duct mesh structure. The plane of symmetry is omitted in this picture.

of such an approach is discussed in [5]. The computational grid for the duct is completely structured, but coupling the mesh inside the duct with the space over the ridge and outside is problematic because the interface between the entrance and the free far-field contains different grid patterns. Thus, unstructured cells have been applied to fill this volume. Figures 8–11 illustrate the mesh structure, and Figure 10 provides a close-up view of the unstructured block. In order to compare the two cases, the mesh of the duct section and its AIP is the same for both cases. The unstructured grid volume for the interface between the inside and outside of the duct has been used for the inlet without the ridge to minimize the difference between computational domains. The number of cells for these symmetric domains is more than 4.4 million.

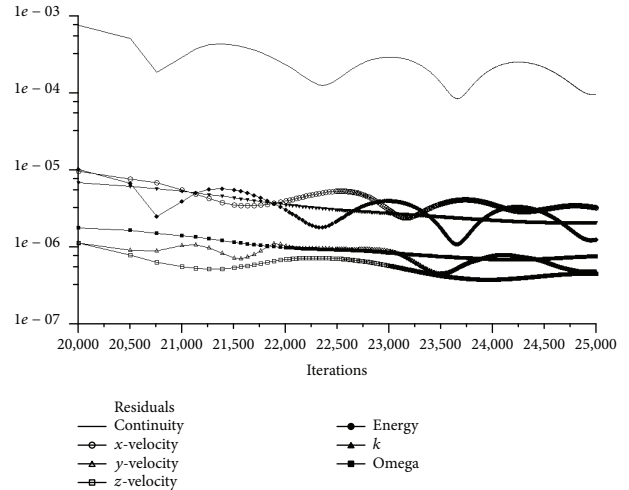


FIGURE 12: Residual condition at the accepted accuracy.

TABLE 2: Main grids in CFD simulations.

Grid	Cell number (million)	P_{t-AIP} (Pa)
M1 (method 1)	0.91	128,679.9
M2 (method 1)	2.47	118,892.1
N1 (method 1)	4.26	117,486.3
N2 (method 1)	5.26	117,579.1
N3	5.81	117,581.8
N4 (results are presented in the current paper, method 1)	6.38	117,589.6
N5 (different internal mesh structure)	6.48	117,585.3

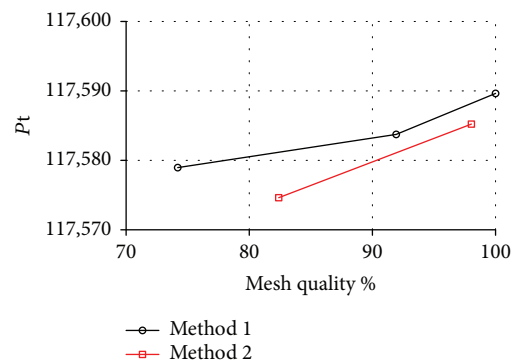


FIGURE 13: Variation of total pressure for fine grids.

4.5. *Grid Study.* Grid dependency is evaluated using different mesh structures. The main cases for which results are considered in this paper contain more than 6.38 million cells for the ridge/inlet configuration. Lower density meshes (more than 4.0 million) can also reach the desired accuracy if the boundary layer block remains dense. The pressure distribution on a cross-section of the duct is selected for comparison. Figure 12 shows the results, and Table 2 compares the calculated total pressures at the AIP for different cases at $M = 0.50$ by the mass-averaged integral formulation. In this table, M1 and

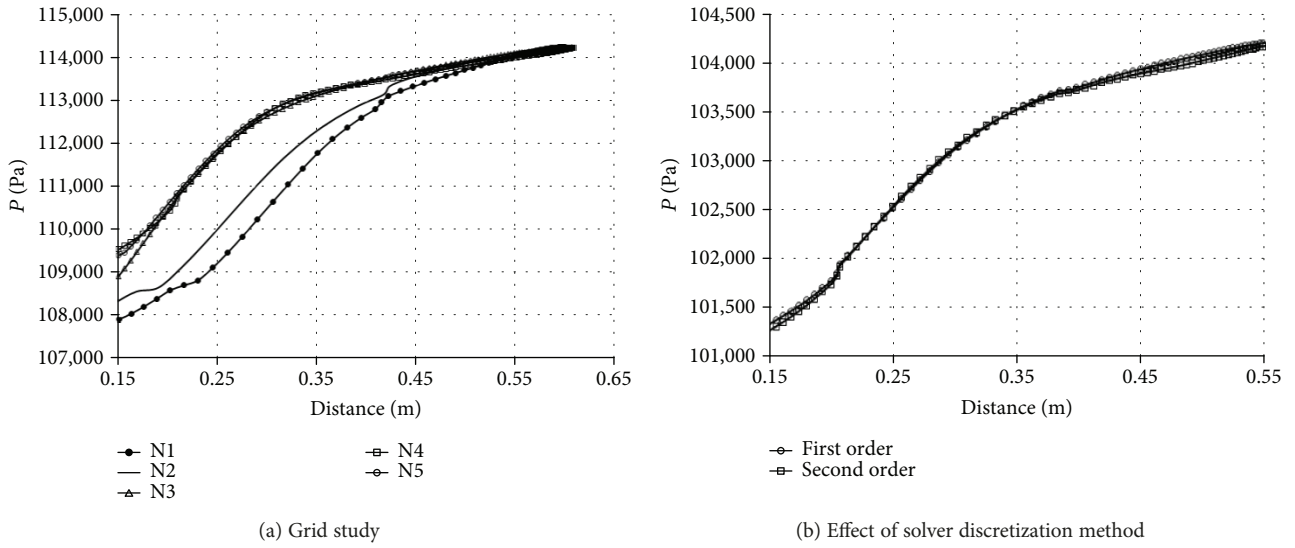


FIGURE 14: Pressure distribution on a longitudinal cross-section at lower surface of diffuser.

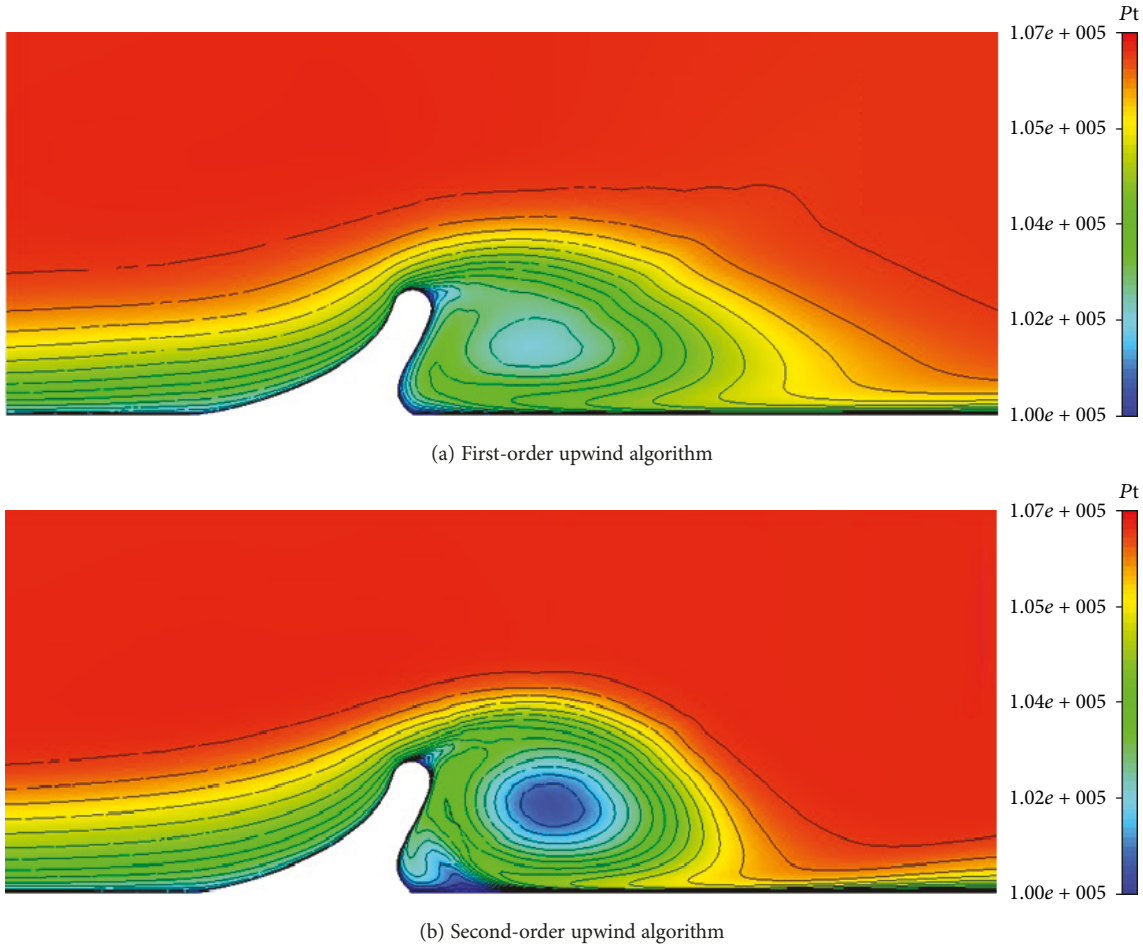


FIGURE 15: Effect of discretization scheme on the vortex structure.

M2 are very light grids with the lowest accuracy, and N1 to N5 are dense grids with accurate results.

Table 2 shows that the difference between measured factors is not significant for N3 and N4. Lighter domains like N1

cannot predict the boundary layer accurately with the $k-\omega$ turbulence model, especially when the boundary layer block is not constant among the study cases. Figure 12 illustrates the residuals condition after 25,000 iterations. This accuracy

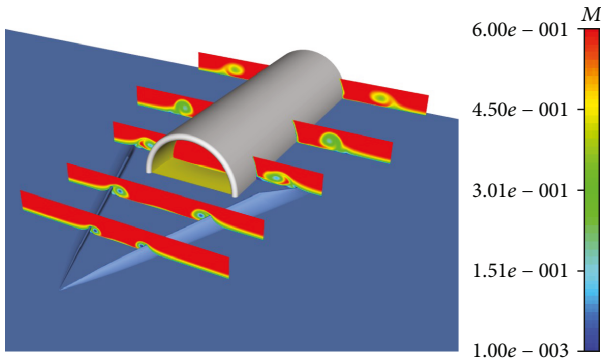


FIGURE 16: Perspective view of ridge/inlet with total pressure contours at different sections $M = 0.5$. This pattern has been repeated for other Mach numbers.

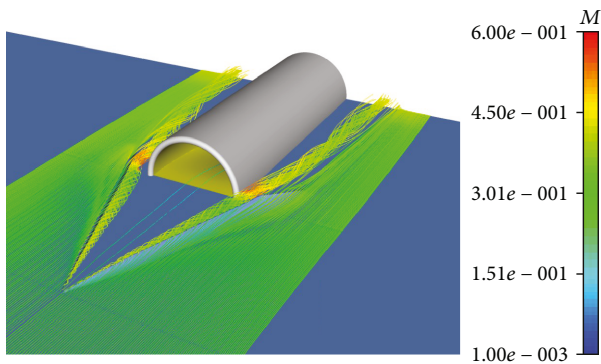


FIGURE 17: Streamlines close to the flat surface, released from upstream, $h = 1.0$ (mm).

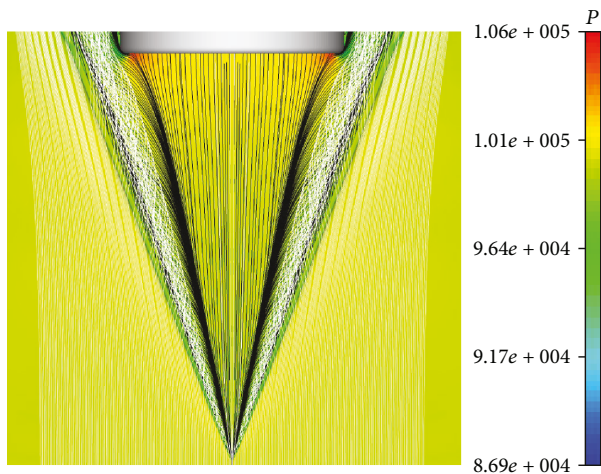


FIGURE 18: Oil pattern in black and the vortex in white color, $M_\infty = 0.3$.

has been considered for all cases. Method 2 represents another grid generation approach with a lighter boundary layer block which the mesh structure of the core flow inside the inlet is relatively denser than the grid blocks of method 1. Figure 13 shows the variation of measured mean total pressure at the AIP for the two approaches.

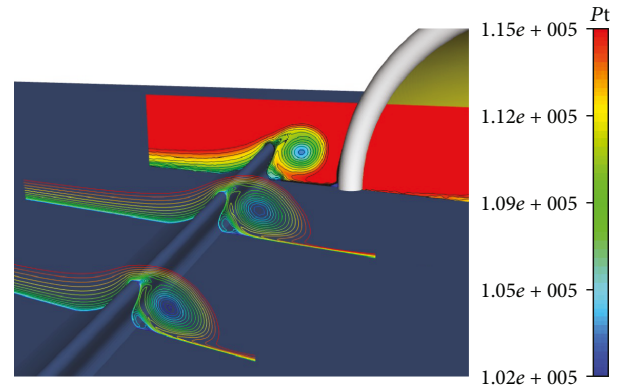


FIGURE 19: Close-up view of total pressure contours before and at the passage, $M_\infty = 0.50$. This pattern is repeated for all subsonic speeds.

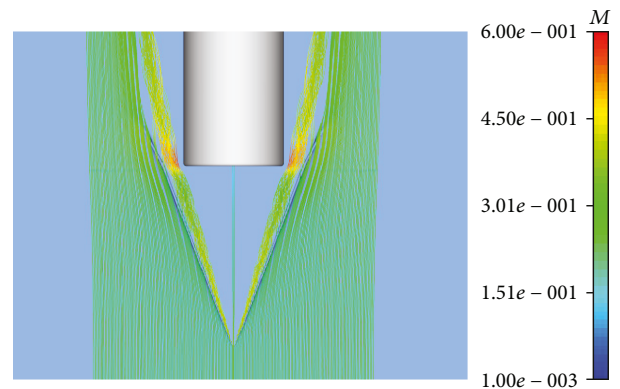


FIGURE 20: Top view of the ridge/inlet configuration, $M_\infty = 0.50$.

The effect of the grid domain on the resultant pressure distribution is shown in Figure 14. After N3, the grid domains provide similar results when residuals exceeds 10^{-6} .

For the dense grid domain (N4), changing the solver discretization algorithm from the first-order to second-order upwind (after 20,000 iterations) does not result in significant changes in the internal pressure distribution after reaching 10^{-6} . This is illustrated by comparing the pressure distribution on the centerline of the lower diffuser wall as shown in Figure 14(b). But the external vortex pattern shows some differences. In both cases, the vortex passes the inlet without breakdown (for subsonic flow) but a second-order discretization algorithm results in higher vortex resolution and details. For the simple flow structures that are aligned with the grid, the numerical diffusion will be naturally low; therefore, it is possible to use the first-order scheme without any significant loss of accuracy. But for the current study, the complex vortex pattern and its interaction with the boundary layer should be simulated accurately to find the possible vortex breakdown or boundary layer separations inside the duct; therefore, using a less dissipative scheme like the second-order upwind is a requirement. The effect of solver order can be seen in Figure 15 by a comparison between cross-sectional total pressure contours.

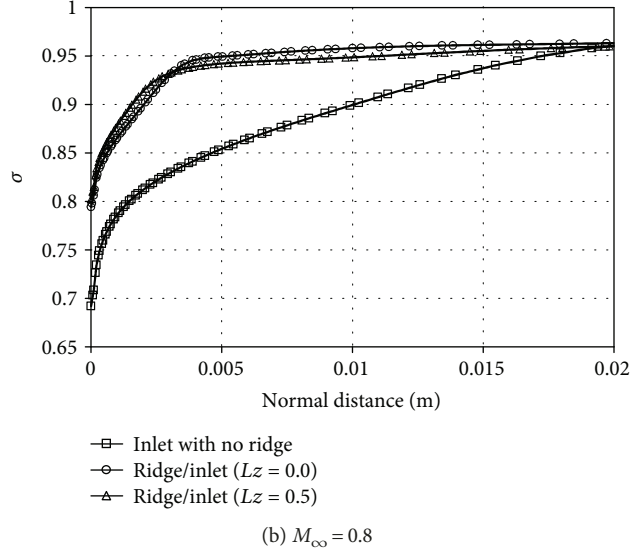
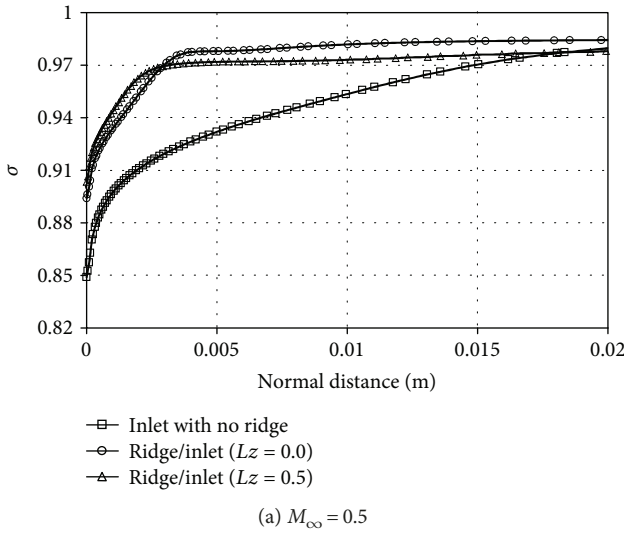


FIGURE 21: Vertical total pressure ratio distribution.

TABLE 3: Duct flow parameters.

M	σ inlet	σ for inlet/ridge	DC ₆₀ for ridge/inlet	DC ₆₀ for inlet without ridge	M_f (%)
0.3	0.991	0.991	0.034	0.351	~0.0
0.5	0.981	0.985	0.040	0.239	5.1
0.8	0.979	0.989	0.110	0.262	12.7

5. Results and Discussions

For the inlet configuration without upstream ridges, simulations show that the duct flow contains turbulence and three-dimensionalities even at low subsonic speeds ($M = 0.3$). The boundary layer developed from the upstream surface results in significant flow separation inside the duct. In contrast, the flow conditions for the ridge/inlet combination are completely different, and details are described in the following subsections. Optimizing the geometry transition algorithm between the entrance profile and the compressor face can improve the internal flow quality to some extent although duct optimization is not a goal in this study.

5.1. Flow Pattern and Diverting Ability of the Ridge. The vortex structure is indicated by the total pressure contours in Figure 16. Contours show that the vortex is stable and passes through the vortex passage without any significant deformation. Over 90% of the low-kinetic-energy boundary layer is captured by the vortex in the regime $0.2 < M < 0.8$. No breakdown or detachment from the LPS has been observed at different Mach numbers along the ridge. Figure 16 shows that the vortex detaches from the end of the ridge and continues its path parallel to the freestream direction to the end of the flat surface. A dense group of streamlines, released above the flat surface, is shown in Figure 17. Simulation results show that a large fraction of the streamlines is captured by the ridge vortex and directed

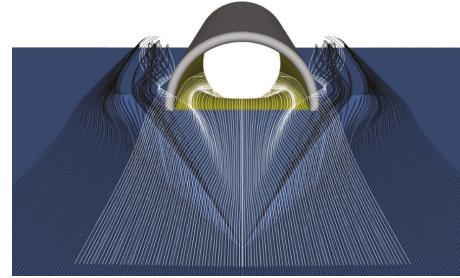


FIGURE 22: Black streamlines at $h = 1$ (mm) and white streamlines at $h = 50$ (mm) over the surface, $M_\infty = 0.80$.

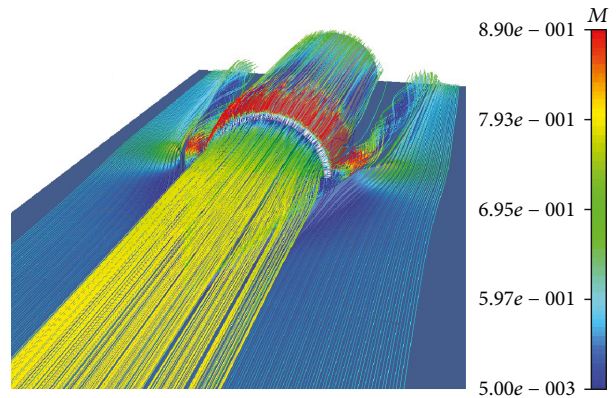


FIGURE 23: Flow pattern at $M_\infty = 0.80$.

into the passage. This pattern has been observed for all Mach numbers evaluated.

As was expected, the inlet entrance is completely protected from the boundary layer developed from upstream. On some parts close to the vortex region on the central surface, the boundary layer is swept by the vortex. Oil patterns in Figure 18 illustrate this phenomenon clearly. As Mach number increases, the vortex core starts to approach the concave profile of the LPS. This property of the flow is important

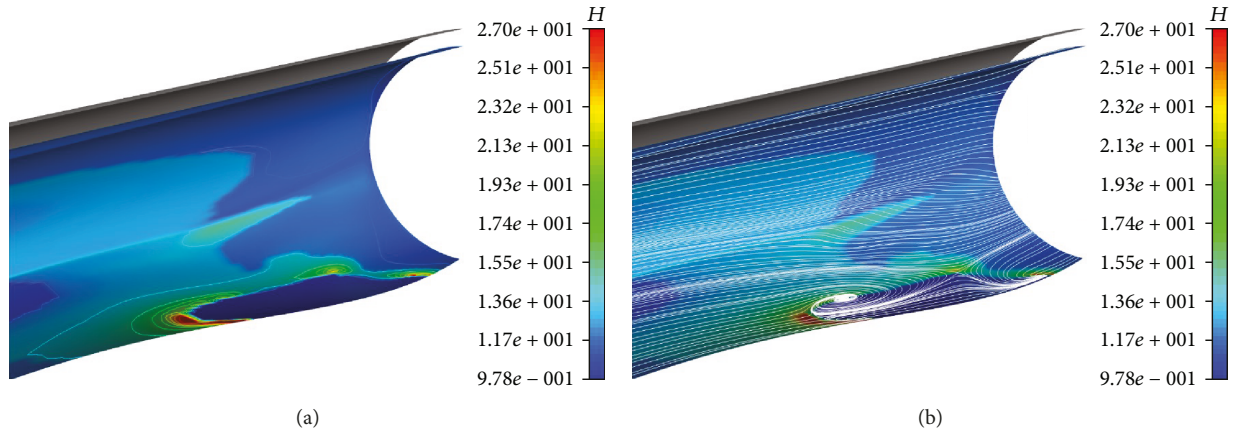


FIGURE 24: H contours on the diffuser surface, $M = 0.8$. Around the separation regions, H has the highest values.

TABLE 4: Shape factor and flow separation coordinate.

M	H_{\max} for inlet	H_{\max} for ridge/inlet	x_1 for inlet	x_1 for ridge/inlet
0.3	3.501	2.341	0.156	—
0.5	3.068	2.481	0.177	—
0.8	3.804	2.663	0.203	0.139

in keeping and controlling the vortex in the low-pressure zone of the ridge.

5.2. Vortex/Passage Interaction. Flow quality at the inlet entrance is an important attribute for ridge/inlet integration. The passage between ridge and inlet should let the vortex pass away safely, and any vortex breakdown should happen after this passage. Figure 19 illustrates the vortex structure with total pressure contours before and at the passage at $M_{\infty} = 0.50$. This pattern has been repeated in the subsonic to transonic Mach range. No breakdown has been observed along the ridge's LPS, and at the passage, the vortex structure is more circular. It appears that the vortex is compressed by the high-pressure zone around the inlet lip. The passage that is formed by the rear profile and the inlet lip section creates a convergent-divergent region for the vortex. As the vortex reaches to the end of the ridge, it is accelerated before the expansion region at subsonic to transonic speeds. Increasing the Mach number at this location can be seen in Figure 20 where the streamline colors are changed (from green to red at the passage).

Downstream of the ridge, the vortices that it generates provide a small amount of additional lift, and the rear part of the ridge plays an important role in controlling the vortex structure. In contrast to [1], for the top-mounted inlet configuration, it is preferable to let the vortex remain attached to the rear part of the fuselage.

5.3. The Flow Quality for the Inlet. Apart from the CFD flow visualization, the flow quality can be measured by the total pressure ratio (σ). This ratio measures the energy losses in the boundary layer. Figures 21(a) and 21(b) illustrate the variation of this factor with the vertical distance near the surface

just before the entrance of the inlet. From these diagrams, it is clear that the boundary layer captured by the ridge/inlet configuration inlet has losses that are less than that of the free inlet on the flat surface.

Another interesting difference between the concepts is the captured mass flow rate. Mass flux calculations at the AIP show that the captured mass flow ratio in the transonic mode is much higher for the ridge/inlet configuration. The calculation results are summarized in Table 3. This ability can be explained by the ridge flow pattern. The ridge diverts the boundary layer but upper layers of flow with higher kinetic energy are guided into the entrance under the effect of the ridge vortical flow pattern. This passive mechanism is illustrated by Figure 22 for a freestream value of $M = 0.8$ where the streamlines in the boundary layer ($h = 1$ mm) are in black and the streamlines above the surface are white. Figure 23 shows the flow pattern by dense streamlines.

When the high-speed layers of the flow pass over the vortices, they are guided downward into the central surface and inlet. This kind of inlet feeding is still under study in our research.

5.4. Internal Performance. With the effective diversion of the boundary layer before the intake entrance, the secondary flow separation problem has been solved for subsonic to transonic speeds. The ridge captures the low kinetic energy layers of the flow close to the surface, so that the fresh flow spills into the entrance. The thinner boundary layer after the ridge is more stable and can resist the adverse pressure gradient inside the duct. This issue can be studied by the shape factor (H) distribution inside the duct for different cases. Generally, for $H > 2.6$, the boundary layer flow separation on the surface should be expected. The maximum value of H is the criterion as to whether flow separation has occurred or not. Results show that at $M = 0.8$, there is a local flow separation in a region (for ridge/inlet configuration), and Figure 24(a) illustrates this region by the H distribution contours.

The oil pattern in Figure 24(b) shows the separation area clearly. This vortical pattern reattaches to the surface after a short distance before the AIP. At lower Mach numbers, there is no separation. Table 4 contains the maximum value of the

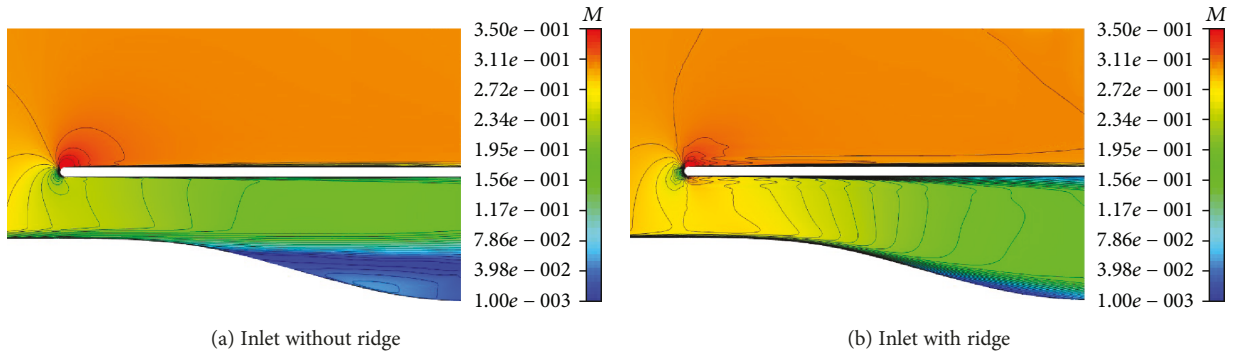
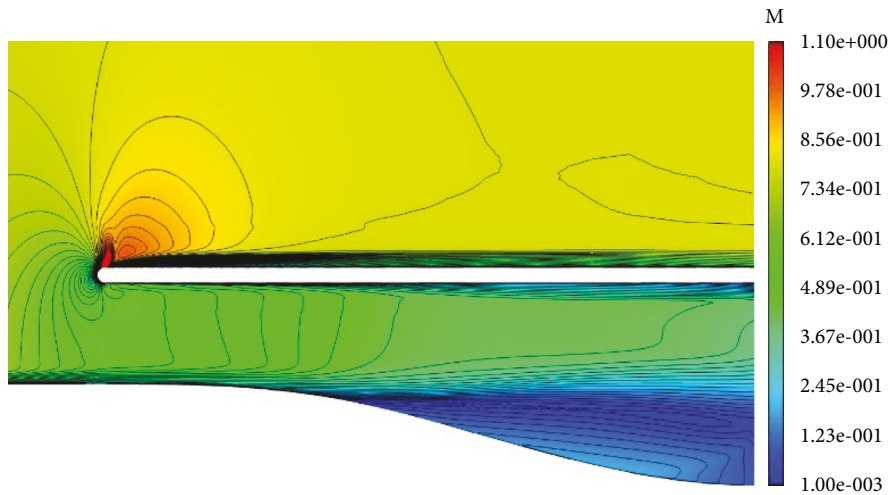
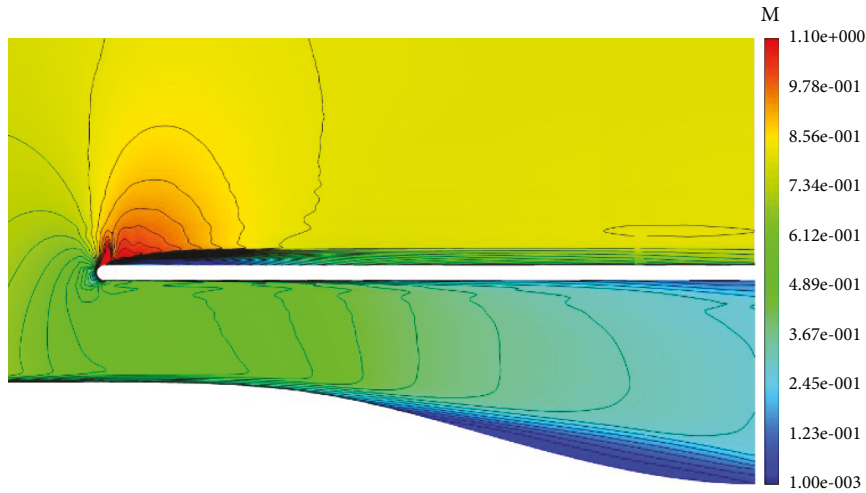


FIGURE 25: Mach contours on the plane of symmetry at $M_\infty = 0.3$.



(a) Inlet without ridge



(b) Inlet with ridge

FIGURE 26: Mach contours on the plane of symmetry at $M_\infty = 0.8$.

shape factor (H_{max}) inside the duct for the inlet with and without the ridge. Note that the boundary layer inside the inlet without the ridge is fully separated for $0.3 < M_\infty < 0.8$. Mach contours in Figure 25(a) show the detached flow inside the duct whereas the conditions for ridge/inlet combination in Figure 25(b) are totally different at $M_\infty = 0.30$.

Comparison between the Mach contours also shows the thickness of swallowed boundary layer. Figures 26(a) and 26(b) make such a comparison for the transonic phase, and Figures 27(a) and 27(b) provides a close-up view of the detached flow region. At the same back pressure, the ridge/inlet configuration retains good performance whereas the

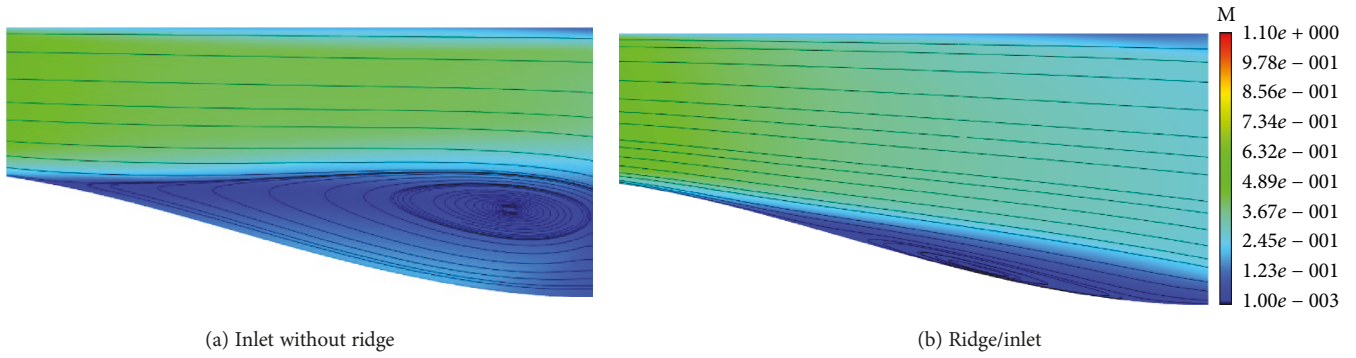


FIGURE 27: Close-up view of tangential streamlines on the plane of symmetry at $M_{\infty} = 0.8$.

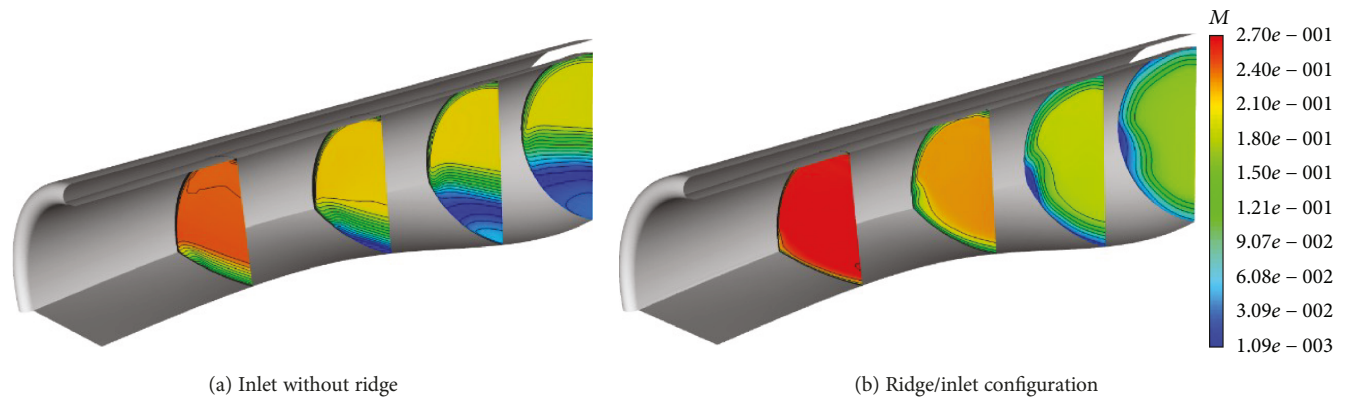


FIGURE 28: Mach contours at different sections at $M_{\infty} = 0.3$.

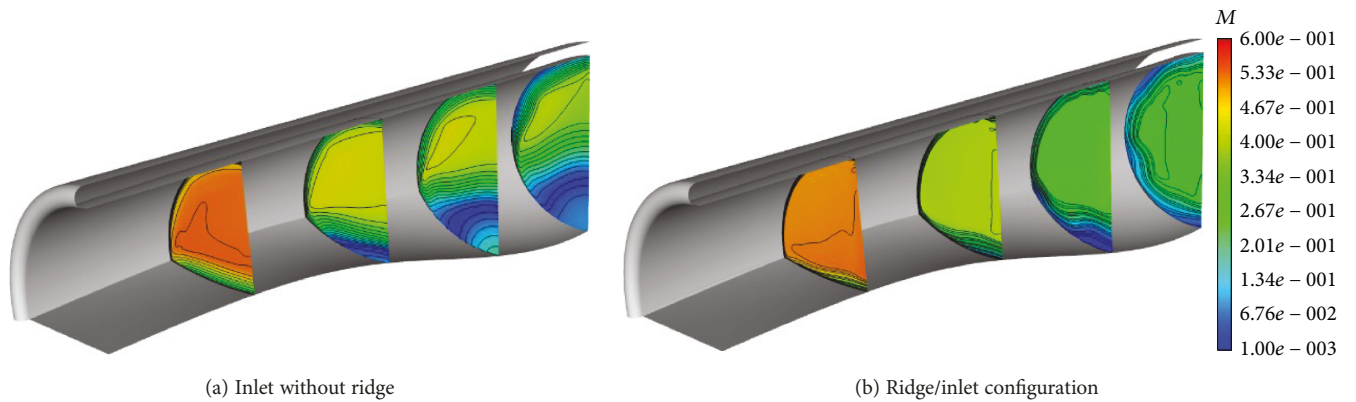


FIGURE 29: Mach contours at different sections at $M_{\infty} = 0.8$.

free inlet does not. Figures 28 and 29 provide perspective views of cross-sectional Mach contours for comparison.

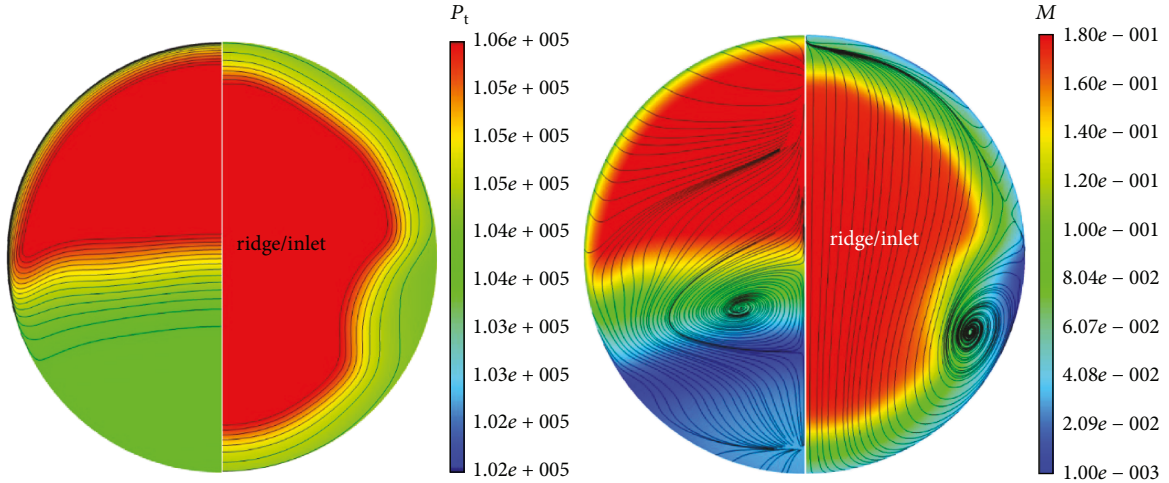
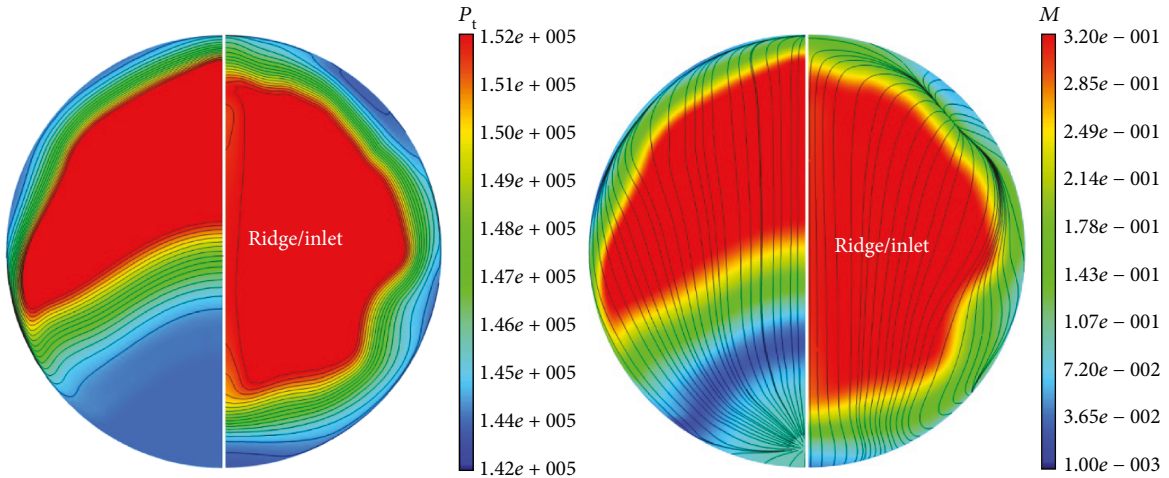
A comparison between the AIP total pressure and Mach number distributions in Figures 30 and 31 shows significant flow improvement for the ridge/inlet configuration. As mentioned before, even at low subsonic speeds, the boundary layer inside the basic inlet detaches from the surface due to the adverse pressure gradient which is applied by the AIP.

Tangential streamlines in Figures 30 and 31 show a vortical pattern at the AIP. For the inlet without the ridge, this pattern was expected. For the ridge/inlet geometry, the transition between the sharp corners of the entrance

to the circular AIP is the main reason for the generation of this pattern. With increasing Mach number, this pattern shifts to the lower sections of the AIP and for $M > 0.5$, the vortical pattern of tangential streamlines can no longer be observed.

The numerical solution was analyzed at the AIP with respect to overall performance factors such as total pressure recovery (σ) and distortion coefficients (DC_{60}) with the following formulations.

$$\sigma = \frac{P_{t-AIP}}{P_{t-\infty}}, \quad (13)$$

FIGURE 30: Total pressure and Mach contours at the AIP, $M_\infty = 0.3$.FIGURE 31: Total pressure and Mach contours at the AIP, $M_\infty = 0.8$.

$$DC_\theta = \frac{P_{t-AIP} - P_{t-\theta}}{q_{AIP}} \quad (14)$$

In these equations, the P_{t-AIP} is the mean total pressure at the AIP, $P_{t-\infty}$ is the freestream total pressure, $P_{t-\theta}$ is the mean total pressure in the “worst” sector of the AIP face, and q_{AIP} is the mean dynamic pressure of the AIP. θ is the length of the arc of each sector. These results are presented in Table 3. M_f represents the increment of mass flow rate at the AIP.

The results in Table 4 indicate that by increasing the Mach number, the effect of the ridge on the total performance of the inlet increases simultaneously. Figures 32(a) and 32(b) show a comparison between the inlets on a flat plate and an inlet without boundary layer ingestion.

5.5. Supersonic Regime Performance. Although the inlet with a uniform large lip radius profile in this analysis is not designed for supersonic applications, in this section, the effect of ridge on the shock structure of the inlet is discussed

based in the CFD results. The Mach number for the simulation is 1.50, and ambient pressure is 100,000.0 Pa.

By applying back pressure (P_b) equal to 2.4×10^5 Pa, a three-dimensional bifurcated shock appears in front of the inlet. For the pitot inlet, the detached normal shock is important because it can result in strong vortex/shock interactions. Figure 33 shows this shock with transparent isosurfaces. The vortex enters to the side section of the conical shape structure of the shock wave and interacts with the chaotic flow pattern at the shock root. According to the streamlines in this figure, the vortex/shock interaction does not result in the fully expanded vortical structure after or inside the shock region. Figure 34 illustrates the vortex core path through the shock wave. The vortex core passes through the shock wave safely, but the vortical pattern changes its shape to a more uniform flow after the ridge. Such a behavior can be recognized as a vortex breakdown. In addition to the detached shock wave, the interaction between the vortex and rear profile and also the expansion region close to the rear profile can be the

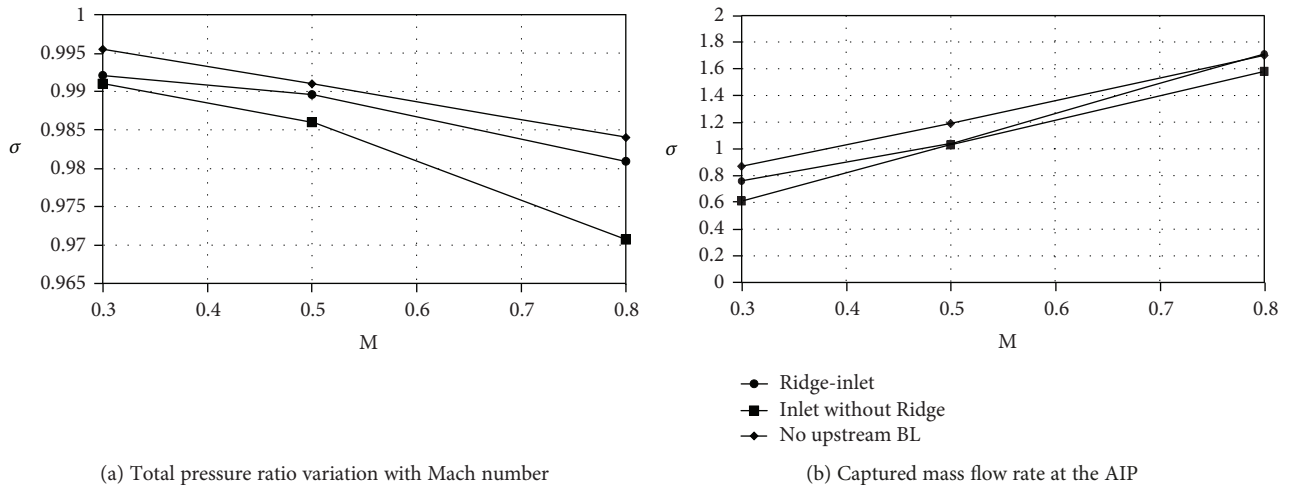


FIGURE 32: AIP calculations.

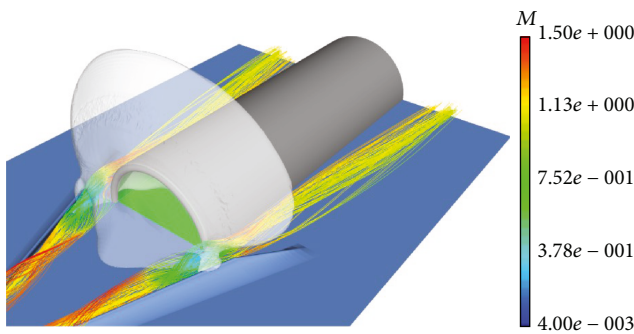


FIGURE 33: Perspective view of the detached normal shock (bifurcated shock) at the entrance.

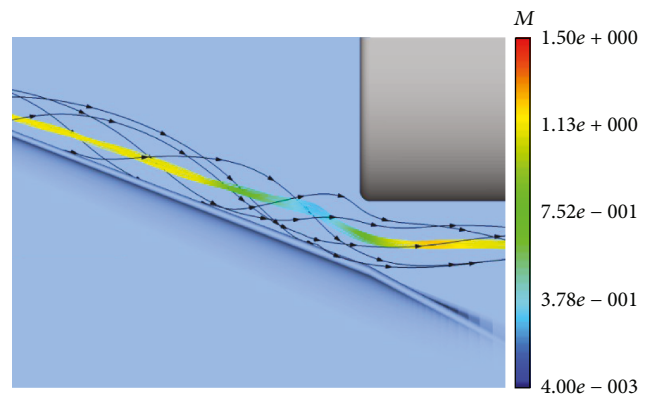


FIGURE 34: Close-up view of the vortex passing through the shock wave.

reason for a uniform pattern. Although the inlet is saved from the vortex, flow separation inside of the inlet is inevitable after the normal shock.

The ridge can be used with a supersonic pitot inlet when the inlet contains very smooth curvature, sharper lips, and long length to let the separated flow reattach to the surface. When the normal shock is placed at the lip (critical mode), the vortex/shock interactions are minimized. Figure 35 presents a better ridge/inlet combination for supersonic applications. Other ridge concepts for high speed usage can be found in [23].

6. Conclusion

The effects of the ridge concept on the performance of a highly integrated inlet are investigated in this paper. The ridge structure contains neither a bleed system nor movable parts, and it can be integrated with different shapes of inlets. CFD simulations show that ridge can redirect the boundary layer based on two aerodynamic phenomena: pressure gradient on its surfaces and vortices. The combination of pressure reduction and vortices creates an effective trap to redirect low energy boundary layer at different Mach numbers. According to these CFD simulations, the basic ridge/inlet configuration shows a practicable passive solution over a wide range of

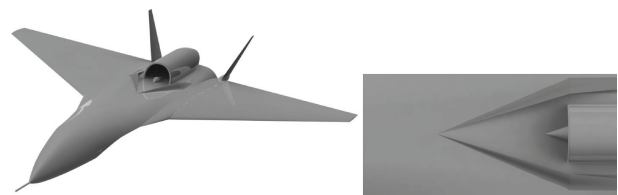


FIGURE 35: Cone compression surface for ridge/inlet configuration.

subsonic to low supersonic Mach number. In the current design, the central surface does not play a significant role in boundary layer diverting. Adding an extra compression geometry or bump surface and redesigning the entrance for supersonic conditions may improve the diverting ability and propulsion efficiency. Results of simulations show that the new concept provides a higher value of pressure recovery in comparison with other submerged or highly integrated inlet combinations. By effective diversion of the upstream boundary layer, ridge provides air with higher kinetic energy and thinner boundary layer for the inlet which prevents or reduces boundary layer separation at speeds up to the high subsonic region. The inlet has also been considered for supersonic study. According to these results, the vortex has a weak

interaction with the bifurcated shock wave in front of the entrance. The shock/vortex interaction is located at the shock root which is attached to the boundary layer, and the vortex core leaves the ridge profile without entering into the inlet.

Nomenclature

BL:	Boundary layer
DC_{θ} :	Distortion coefficient based on θ -degree sectors
SST:	Shear stress transport
AIP:	Aerodynamic interface plane
E :	Total energy
P :	Static pressure
P_b :	Back pressure
P_t :	Total pressure
P_t^* :	Turbulent Prandtl number
$P_{t\infty}$:	Freestream total pressure
$P_{t-\theta}$:	Sectorial mean total pressure at AIP
q_{AIP} :	Mean dynamic pressure at AIP
σ :	Total pressure recovery coefficient
τ_{ij} :	Stress tensor
M :	Mach number
M_f :	Increment of mass-flow ratio coefficient
M_{∞} :	Freestream Mach number
H :	Boundary layer shape factor
H_t :	Total enthalpy
h :	Normal distance from the surface
l_z :	Ratio of the distance from plane of symmetry to the width of the inlet
k :	Turbulence kinetic energy
k_A :	Averaged turbulence kinetic energy at AIP
μ :	Viscosity coefficient
μ_l :	Laminar viscosity coefficient
μ_t :	Turbulent viscosity coefficient
ω :	Turbulence dissipation rate
x_i :	Length ratio of separation point
i, j, k :	Counter variables
u_1, u_2, u_3 :	Velocity components in x, y, and z directions
ρ :	Density
G_k :	Production term of k
Y_k :	Dissipation term of k
Γ_k :	Diffusion term of k
G_{ω} :	Production term of ω
Y_{ω} :	Dissipation term of ω
Γ_{ω} :	Diffusion term of ω
S_h :	Source term vector
e :	Internal energy
h_s :	Static enthalpy.

Data Availability

The data used to support the findings of this study are available from the corresponding author upon request.

Conflicts of Interest

The authors declare that they have no conflicts of interest.

Acknowledgments

Inlet team members in the College of Power and Energy of NUAA are gratefully acknowledged for their cooperation. This research is supported by National Basic Research Program of China (No. 2014CB239602) and Natural Science Foundation of China (No. 11372134).

Supplementary Materials

The flow pattern of the ridge surface is evaluated by a series of wind tunnel tests in NUAA. The vortex structure and its stability are studied. No breakdown or vortex core distortion was visualized during the low subsonic tests. The stability of vortex in low subsonic flow was our main concern during ridge/inlet integration. (*Supplementary Materials*)

References

- [1] E. B. Saheby, H. Gouping, Q. Wenyong, and T. Weiyan, "Highly integrated inlet design based on the ridge concept," *Journal of Propulsion and Power*, vol. 32, no. 6, pp. 1505–1515, 2016.
- [2] E. L. Goldsmith and J. Seddon, *Practical Intake Aerodynamic Design*, AIAA Education Series, Chaps. 1, 3, AIAA, 2nd edition, 1993.
- [3] J. Seddon and E. L. Goldsmith, *Intake Aerodynamics*, AIAA Education Series, Chaps. 2, 3, AIAA, New York, 2nd edition, 1999.
- [4] C. Fiola and R. K. Agarwal, "Simulation of secondary and separated flow in diffusing S ducts," *Journal of Propulsion and Power*, vol. 31, no. 1, pp. 180–191, 2015.
- [5] T. M. Berens, A.-L. Delot, M. Tormalm, L.-P. Ruzi, and D. E. Funes-Sebastian, *Numerical and Experimental Investigations on Highly Integrated Subsonic Air Intakes*, AIAA Scitech, National Harbor, MD, USA, 2014.
- [6] "General atomic aeronautical," May 2018, <http://www.ga-asi.com>.
- [7] "NASA," May 2018, <http://www.nasa.gov>.
- [8] "Global security," May 2018, <http://www.globalsecurity.org>.
- [9] "Wikipedia," May 2018, <http://www.wikipedia.org>.
- [10] R. K. Scharnhorst and A.-L. Delot, "Computational and experimental results for flow in a diffusing S-duct without and with flow control devices," in *51st AIAA/SAE/ASEE Joint Propulsion Conference*, pp. 27–29, Orlando, FL, USA, 2015.
- [11] S. Lei and R. W. Guo, "Serpentine inlet design and analysis," in *50th AIAA Aerospace Sciences*, Nashville, TN, USA, 2012.
- [12] G. Huang, E. B. Saheby, M. Akhlaghi, and Z. Yu, "Effects of ridge configuration on the performance of integrated inlets," in *52nd AIAA/SAE/ASEE Joint Propulsion Conference*, Salt Lake City, UT, USA, 2016.
- [13] Y. Ito, K. Yamamoto, K. Kusunose et al., "Effect of vortex generators on transonic swept wings," *Journal of Aircraft*, vol. 53, no. 6, pp. 1890–1904, 2016.
- [14] F. R. Menter, M. Kuntz, and R. Langtry, "Ten years of industrial experience with the SST turbulence model," *Turbulence, Heat and Mass Transfer*, vol. 4, no. 1, pp. 625–632, 2003.
- [15] R. C. Nelson and A. Pelletier, "The unsteady aerodynamics of slender wings and aircraft undergoing large amplitude maneuvers," *Progress in Aerospace Sciences*, vol. 39, no. 2-3, pp. 185–248, 2003.

- [16] K. Yamamoto, K. Tanaka, and M. Murayama, "Effect of a non-linear constitutive relation for turbulence modeling on predicting flow separation at wing-body juncture of transonic commercial aircraft," in *30th AIAA Applied Aerodynamics Conference*, New Orleans, Louisiana, USA, June 2012.
- [17] *Fluent 6.3 User's guide*, Fluent Inc, New York, NY, USA, 2006.
- [18] D. Rockwell, "Vortex-body interactions," *Annual Review of Fluid Mechanics*, vol. 30, pp. 199–229, 1998.
- [19] F. R. Menter, "Two-equation Eddy-viscosity turbulence models for engineering applications," *AIAA Journal*, vol. 32, no. 8, pp. 1598–1605, 1994.
- [20] T. J. Barth and D. Jespersen, "The design and application of upwind schemes on unstructured meshes," in *27th Aerospace Sciences Meeting*, Reno, NV, USA, 1989.
- [21] J. M. Weiss, J. P. Maruszewski, and W. A. Smith, "Implicit solution of the Navier-Stokes equations on unstructured meshes," in *13th Computational Fluid Dynamics Conference, Fluid Dynamics and Co-located Conferences*, Snowmass, CO, USA, July 1997.
- [22] P. L. Roe, "Approximate Riemann solvers, parameter vectors, and difference schemes," *Journal of Computational Physics*, vol. 135, no. 2, pp. 250–258, 1997.
- [23] E. B. Saheby, G. Huang, W. Qiao, and W. Tang, "A novel compression surface for integration design of high speed aircraft forebody and inlet," in *20th AIAA International Space Planes and Hypersonic Systems and Technologies Conference*, Glasgow, Scotland, 2015.

